RESEARCH ARTICLE
Editor's Choice
ADVANCED MATERIALS INTERFACES Open Access
www.advmatinterfaces.de

Check for updates

Direct Measurements of Anisotropic Thermal Transport in γ-InSe Nanolayers via Cross-Sectional Scanning Thermal Microscopy

Sergio Gonzalez-Munoz, Khushboo Agarwal, Eli G. Castanon, Zakhar R. Kudrynskyi, Zakhar D. Kovalyuk, Jean Spièce, Olga Kazakova, Amalia Patanè, and Oleg V. Kolosov**

Van der Waals (vdW) atomically thin materials and their heterostructures offer a versatile platform for the management of nanoscale heat transport and the design of novel thermoelectrics. These require the measurement of highly anisotropic heat transport in vdW-based nanolayers, a major challenge for nanostructured materials and devices. In the present study, a novel effective method of cross-sectional scanning thermal microscopy was used to map and quantify the anisotropic heat transport in nanoscale thick layers of vdW materials and the material-substrate interfaces. This technique measures the heat conducted into a vdW crystal via the nanoscale apex of a heat-sensitive probe. The crystal is nano-polished via Ar ion beams generating an oblique nearly atomically flat surface. By measuring the thermal conductance variation as a function of increasing layer thickness, the transition between the cross-plane and in-plane heat transport (defined by heat conductivity anisotropy) is acquired. By using an analytical model validated by finite element simulations, anisotropic thermal transport in a gamma indium selenide crystal nano-thin flake on a Si substrate was studied, obtaining results corresponding to anomalously low anisotropic thermal conductivities of k_{xy} = 2.16 Wm^{-1} K^{-1} in-plane and k_z = 0.89 Wm^{-1} K^{-1} cross-plane confirming its potential for thermoelectric applications.

1. Introduction

The unique properties of atomically thin 2D materials (2DMs) include versatile electronic band structures, ultimate mechanical strength, and record both high and low thermal conductivities.[1–4] Van der Waals (vdW) stacked heterostructures allow efficient tuning of these properties, opening multiple applications in diverse areas.[5–8] Varying the thickness and geometrical arrangement of the constituent atomic layers enables the engineering of both electrical and thermal conductivities.[9–14] In turn, this allows the use of vdW materials as promoters of heat dissipation in nanostructures,[15,16] providing vitally needed heat spreading in processor chips.[17–19] At the same time, other vdW materials allow to decrease the heat transport in semiconductor structures, a subject of great interest in thermoelectric (TE) applications,[20–24] where thermal conductance that has both electronic and phononic contributions [22] is a detrimental

S. Gonzalez-Munoz, K. Agarwal, O. V. Kolosov
Department of Physics
Lancaster University
Lancaster LA1 4YB, UK
E-mail: s.gonzalezmunoz@lancaster.ac.uk; o.kolosov@lancaster.ac.uk

E. G. Castanon
The University of Manchester, National Graphene Institute
Booth St E, Manchester M13 9PL, UK

Z. R. Kudrynskyi, A. Patanè
School of Physics and Astronomy
University of Nottingham
Nottingham NG7 2RD, UK

Z. D. Kovalyuk
Institute for Problems of Materials Science
National Academy of Sciences of Ukraine
Chernivtsi Branch, Chernivtsi 58001, Ukraine

J. Spièce
Institute of Condensed Matter and Nanosciences
Nanoscopic Physics
Université Catholique de Louvain
Louvain-la-Neuve 1348, Belgium

O. Kazakova
National Physical Laboratory, Quantum Materials and Sensors
Hampton Road, Teddington TW11 0LW, UK

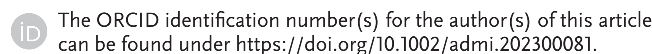
The ORCID identification number(s) for the author(s) of this article can be found under https://doi.org/10.1002/admi.202300081.

© 2023 The Authors. Advanced Materials Interfaces published by Wiley-VCH GmbH. This is an open access article under the terms of the Creative Commons Attribution License, which permits use, distribution and reproduction in any medium, provided the original work is properly cited.

DOI: 10.1002/admi.202300081

phenomenon. Semiconductor materials generally are the most likely candidates for TE devices, given that they possess a band structure that can provide high electrical conductivity and TE Seebeck coefficient, as well as relatively low phonon-dominated thermal conductivity.[25–27] In the search for the ideal material, gamma indium selenide (γ-InSe), a material that can form a series of different allotropes, holds a promise of such a "wonder" thermoelectric candidate, thanks to its direct bandgap, high electrical conductivity, and atomically flat layered structure with interlayer vdW bonds. This semiconductor belongs to a wide family of metal chalcogenide (MC) compounds (M = group-III metals Ga and In; C = group-VI chalcogens S, Se, and Te). They can exist in different stoichiometries, crystal structures, and layer stacking sequences (e.g., In_2Se_3,[28–30] In_2S_3, Ga_2S_3,[28,31] and many others) and exhibit a range of unique physical properties required for modern ultra-thin electronic devices,[32,33] such as ferroelectricity,[34] high mechanical strength and flexibility, thickness-tunable optical band edge absorption,[35,36] photoresponsivity in the broad infrared to the ultra-violet light range,[31,37–39] as well as high electron mobility and low-mass charge carriers that improve the electrical transport in electronic applications and the speed of photoresponse.[40] However, the data on thermal transport characteristics in γ-InSe are very limited [41] compared to those for optical or electrical properties, with the majority of the current knowledge based on a theoretical analysis of the thermal transport in this material and no reports of experimental measurements of thermal transport anisotropy in γ-InSe.[35,41–44]

For experimental studies of thermal transport in nanostructures, scanning thermal microscopy (SThM), a technique that measures the heat flow from a micromachined probe into the sample in contact with its nanoscale apex, is, arguably, the most efficient method to investigate thermal transport at the nanoscale.[45–47] However, the SThM in its current incarnation has major limitations when it comes to quantifying heat transport in anisotropic materials. In fact, the SThM response is strongly convoluted with the tip-sample thermal resistance [48–49] as well as affected by the interfacial thermal resistivity between the material and the substrate. A recent study of γ-InSe using SThM by Buckley et al.[41] revealed a low thermal conductivity for both free-standing InSe layers and layers supported by different substrate materials, such as low thermal conductivity silicon dioxide (SiO_2). The SThM thermal response is influenced by phonon scattering at edges and interfaces of InSe, as well as strain and thermal coupling of the vdW material to its supporting substrate. However, this previous study of InSe neither could quantify the absolute values of thermal conductivity due to the generally unknown tip-sample and sample-substrate interfacial thermal resistances, nor evaluate the thermal conductivity anisotropy. With SThM studies conducted in air in this Buckley et al. work, an additional unknown was also the through-the-air heat transport, complicating the absolute measurements of the thermal conductivity of the material itself. Importantly, no other SThM study to date has been able to differentiate between in-plane and cross-plane thermal transport in the nanoscale layers of vdW materials.

Here, we address these challenges by employing a novel functional technique called cross-sectional scanning thermal microscopy (xSThM),[49] which uses a beam-exit cross-sectional nano-polishing (BEXP) [49,50] to prepare a nearly atomically-flat low-angle wedge-like cut of the studied material on the relevant substrate. The thermal conductance is then mapped via SThM under high vacuum (HV) conditions, providing the tip-sample heat transport as a function of the layer thickness. We show that the contribution to the heat transport of an anisotropic layer from the in-plane and cross-plane thermal conductivities changes with the layer thickness. The analysis of the experimental data performed via the straightforward "Muzychka–Spièce" fully analytical model [49,51–54] (supported by the detailed finite element analysis [FEA] simulation) allows us to quantify the thermal conductivity along different crystallographic directions. This approach also independently provides the probe-sample interfacial thermal resistance and enables us to estimate the boundaries of the vdW material-substrate interface thermal resistivity. We apply the xSThM technique to study the thermal conductivity of γ-InSe on a Si substrate, highlighting the importance of the substrate in the thermal transport (see Section S7, Supporting Information) and demonstrating that xSThM, with its intrinsic sensitivity to the local heat transport, provides a powerful platform for quantitative studies of γ-InSe or other vdW materials, heterostructures, and relevant devices.

2. Results and Discussion

2.1. Sample Preparation

In order to access the internal layers of our material we use beam exit cross-sectional polishing (BEXP). This technique allows us to create a low-angle wedge cut of the structure with near-atomic roughness.[50] To perform the cut, the flake of interest is deposited close to the substrate's edge (**Figure 1**d), and then, the chip is positioned on a stage that is tilted at a small angle (3–5°) with respect to the horizontal plane (Figure 1a). An etch-resistant mask is positioned on the side of the sample below the chip's surface (Figure 1b). Subsequently, three overlapping co-planar Ar-ion guns create an ion flux that is directed towards the side edge of the sample and that exits through the top surface (hence, the "beam exit" name). The region of the sample that is exposed to the polishing beam is etched away over a period of several hours. With the combination of the non-reactive nature of Ar, the near-glancing incidence angle, and the two-stage post-polishing process at reduced ion energy (Figure 1b and Experimental Section), the final surface presents a near-atomically smooth tilted cut (Figure 1e) with minimal damage.[49,55–58] This process provides perfect access to the substrate, to a range of different thicknesses within the flake, and to the substrate-flake interface, enabling an effective insight into different regions of the exposed surface for the posterior characterization of the thermal transport via SThM (Figure 1c).

2.2. xSThM Heat Transport Measurements

Once the flake and the substrate have been cut, we use a high vacuum SThM (**Figure 2**a) with custom-built thermal measurement electronics (see Section S2, Supporting Information) to measure the heat transport into the sample. During

 © 2023 The Authors. Advanced Materials Interfaces published by Wiley-VCH GmbH

21967350, 0, Downloaded from https://onlinelibrary.wiley.com/doi/10.1002/admi.202300081 by Test, Wiley Online Library on [15/05/2023]. See the Terms and Conditions (https://onlinelibrary.wiley.com/terms-and-conditions) on Wiley Online Library for rules of use; OA articles are governed by the applicable Creative Commons License

21967350, 0, Downloaded from https://onlinelibrary.wiley.com/doi/10.1002/admi.202300081 by Test, Wiley Online Library on [15/05/2023]. See the Terms and Conditions (https://onlinelibrary.wiley.com/terms-and-conditions) on Wiley Online Library for rules of use; OA articles are governed by the applicable Creative Commons License

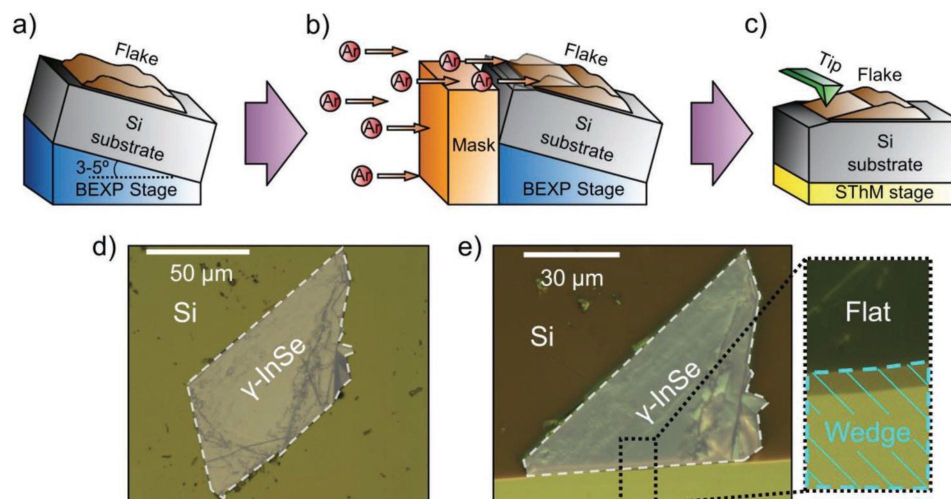

Figure 1. BEXP sample preparation process. a) The sample containing the flake of interest is placed on a custom-built low-angle tilted stage. b) The area of the sample exposed to the argon-ion (Ar-ion) beams (i.e., not shielded by the mask) is etched away. c) The sample is then mounted on the SThM stage for the thermal conductance measurements. d) Optical image of a γ-InSe flake deposited on a Si substrate prior to the BEXP cut. e) Same flake after the BEXP cut. Inset) Zoom of the area with a view of the wedge cut and the top flat surface of the sample.

all the experiments the sample is kept at ambient temperature (300.5 ± 0.2 K) and monitored during the scans with a PT1000 RTD sensor located on the sample stage. Performing the measurements under high vacuum conditions prevented parasitic heat losses via conduction and convection since there are no media in contact other than the tip apex and the sample. In terms of radiation heat losses, proportional to the 4th power of the temperature, these were estimated to be minimal, not affecting the

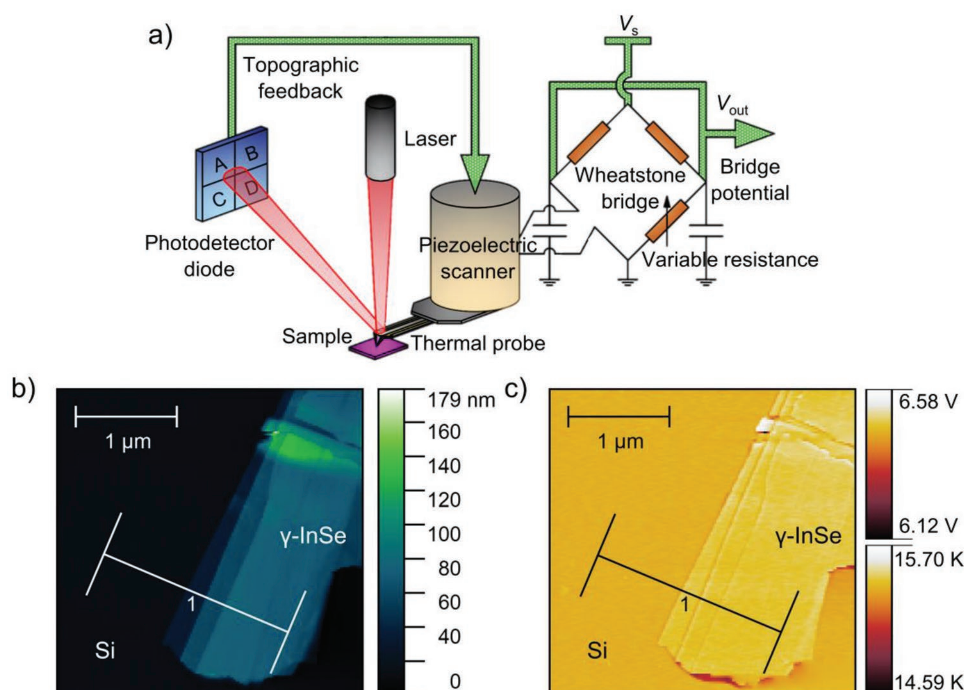

Figure 2. Scanning thermal microscopy (SThM) highlights. a) SThM schematics. The SThM thermal probe incorporates a resistive heater receiving constant power via a DC-AC Wheatstone bridge. The bridge output voltage (i.e., "thermal signal") is used to form the thermal image which is proportional to the probe temperature. This temperature changes due to variations of the probe-sample heat flow, with a lower thermal signal corresponding to the increased heat flow towards the sample, and, hence, to lower thermal resistance between the probe-sample system. By moving the calibrated probe across the sample surface, a quantitative map of the sample heat transport can be obtained. b) Topography and c) thermal signal (top color bar) maps of a γ-InSe flake presenting different thicknesses on a flat Si substrate. The corresponding average probe temperature change limits are also shown on the bottom color bar of the thermal image. Profiles extracted from line 1 in both (b) and (c) are shown in Section S4, Supporting Information.

 © 2023 The Authors. Advanced Materials Interfaces published by Wiley-VCH GmbH

ADVANCED MATERIALS INTERFACES
Open Access
www.advmatinterfaces.de

measurements due to the low absolute temperatures involved in the SThM operation.[59] A platinum resistor incorporated into the SThM probe allows us to resistively heat its apex, which is then brought into contact with the sample surface, normally with lateral dimensions of the apex of a few tens of nanometers across. The heat supplied to the probe is nearly constant, while the probe temperature varies depending on the heat dissipated into the sample and the base of the probe.[46] The probe temperature modifies its electrical resistance which can be measured directly via a DC-AC Wheatstone bridge, producing as an output an SThM "thermal signal" proportional to the variation in the temperature of the probe. Qualitatively, the decrease of the thermal signal corresponds to the increase in the heat flowing onto the sample. After appropriate calibration (see Section S1, Supporting Information), the signal can be converted into the absolute values of the probe-sample thermal resistance.[45,60–62] Further details of the SThM operation are described in the Experimental Section. As an example, Figure 2b,c show the topography and thermal images of a stacked γ-InSe flake with different thicknesses on a flat Si substrate, where a clear change in the topography of the flakes provides only a minor variation in the corresponding thermal signal (see relevant details in Section S4, Supporting Information) that, as shown below, indicates a large tip-sample interfacial thermal resistance.

The SThM tip raster scans the surface of the sample, including the γ-InSe flake and the underlying Si substrate, providing a 2D thermal resistance map of the vdW flake-substrate interface for different values of the vdW material thickness t. In order to calibrate the dimensions of the SThM tip apex and obtain quantitative values of the tip thermal resistance, we use a reference sample composed of a thermally grown 300 nm SiO_2 ($k = 1.4 \pm 0.2$ $Wm^{-1} K^{-1}$) on top of a Si substrate ($k_s = 130 \pm 20$ $Wm^{-1} K^{-1}$) which has been cut following the same procedure explained in the previous section.[63–66]

Figure 3 shows the resulting topography and thermal signal maps of the SiO_2/Si wedge (Figure 3a,b) and γ-InSe/Si wedge (Figure 3e,f) samples. The topographic profiles (Figure 3c,g) along the lines in Figure 3a,e show nearly flat surfaces with a slight change in the slope (≈5%) between the substrate and the top layer. These profiles are used to quantify the thickness ranges of the top layers that vary from 0 to about 100 and 0 to 80 nm for the SiO_2 and the γ-InSe samples, respectively. The surface roughness of the entire 1 µm scans is ≈0.5 nm for the SiO_2 and 6 nm for the γ-InSe layer. This roughness is extracted quantitatively from the flattened topographic maps. However, the local roughness values relevant to the thermal transport through the tip-surface contact, taken from the typical 20–50 nm contact radius size, are 0.5 and ≈1.5 nm for the SiO_2 and γ-InSe, respectively. We note that, while this difference in the surface roughness value of γ-InSe can affect the tip-surface thermal resistance, its scale is much smaller than the overall dimensions of the tip-surface contact, which are typically in the range of 20 to 50 nm,[49] therefore, allowing us to assume that the tip-material contact radius is the same for both materials. Moreover, these low roughness values and minimal surface damage ensure that the BEXP Ar-ion cut does not affect the material's nanomechanical and nanothermal properties, as confirmed elsewhere.[49,57,67,68] Any remaining superficial damage should be homogeneous throughout the exposed surface, not affecting the measurements of the thermal conductivity of the material due to the differential measurement algorithm explained in Section 2.3 below. The resulting slope for both samples is ≈1:6, with the vertical scale being precise up to the sub-nm scale after the calibration of the SThM scanner in the z-direction,[51] allowing us to obtain high precision measurements of the thermal resistance versus the layer thickness. The profiles (Figure 3d,h) of the thermal signal versus position x along the wedge (proportional to the wedge thickness) are taken along the lines shown in Figure 3b,f, distinctly showing the edge of the top material followed by the gradual increase of the thermal signal. A higher thermal signal (proportional to the higher temperature of the probe generated by its Joule heating) indicates a higher thermal resistance of the tip-to-sample contact, which would be expected for the lower thermal conductivity layers (SiO_2, γ-InSe) compared to the higher thermal conductivity of the Si substrate. The observed Al layer in Figure 3f is due to the re-sputtering of the BEXP Al chamber wall by the part of the Ar-ion beam not impinging on the sample. These Al residues can be deposited on the top surface of the sample, whereas the cut that is constantly swept by the Ar beam is not affected. As the measurement data are acquired from the γ-InSe/Si interface well separated from the γ-InSe/Al interface, the Al layer does not contribute to the heat conductance in the area of interest and, hence, to the measured values. The obtained thermal signal profiles are then converted into contact thermal resistance versus thickness data (see Equation (1) and Section S6, Supporting Information), which is ultimately used to obtain the thermal and structural parameters of the γ-InSe with a two-step fitting procedure explained in the next sections.[49,51,52]

The calibration prior to the measurements (see Section S1, Supporting Information) provides values for the probe thermal resistance in vacuum R_p. During the SThM measurements, the out-of-contact V_{nc} thermal signal (independent of the sample thickness) and the in-contact $V_x(t)$ thermal signal as a function of the wedge thickness t at a particular point, are extracted from the thermal signal and topographical profiles (see Section S1, Supporting Information). The thermal resistance $R_x(t)$ of the tip-surface contact is then expressed as:[52]

$$R_x(t) = c_e \frac{V_x(t) R_p}{V_{nc} - V_x(t)} \quad (1)$$

where R_p (1.61×10^5 KW^{-1}) is obtained by calibrating the probe (see Section S1, Supporting Information), and V_{nc} and $V_x(t)$ for γ-InSe/Si and SiO_2/Si are extracted from the thermal signal profiles. Here, c_e is the probe "tooling factor" sensitivity coefficient. It represents a fixed geometric coefficient that accounts for the different thermal signal responses of the probe to the same amount of heat flux while it self-heats (i.e., the value obtained during its calibration), and the heat flux to the sample during the measurements. This factor depends solely on the geometry of the probe and the heater and is independent of the measured sample, or the absolute value of heat applied to the probe (see Section S6, Supporting Information).[51]

The "zero" thickness of the wedge with $t = 0$ nm at position x_0 is determined from the intersection of the lines of the thermal response of the substrate and the top material.

© 2023 The Authors. Advanced Materials Interfaces published by Wiley-VCH GmbH

21967350, 0, Downloaded from https://onlinelibrary.wiley.com/doi/10.1002/admi.202300081 by Test, Wiley Online Library on [15/05/2023]. See the Terms and Conditions (https://onlinelibrary.wiley.com/terms-and-conditions) on Wiley Online Library for rules of use; OA articles are governed by the applicable Creative Commons License

21967350, 0, Downloaded from https://onlinelibrary.wiley.com/doi/10.1002/admi.202300081 by Test, Wiley Online Library on [15/05/2023]. See the Terms and Conditions (https://onlinelibrary.wiley.com/terms-and-conditions) on Wiley Online Library for rules of use; OA articles are governed by the applicable Creative Commons License

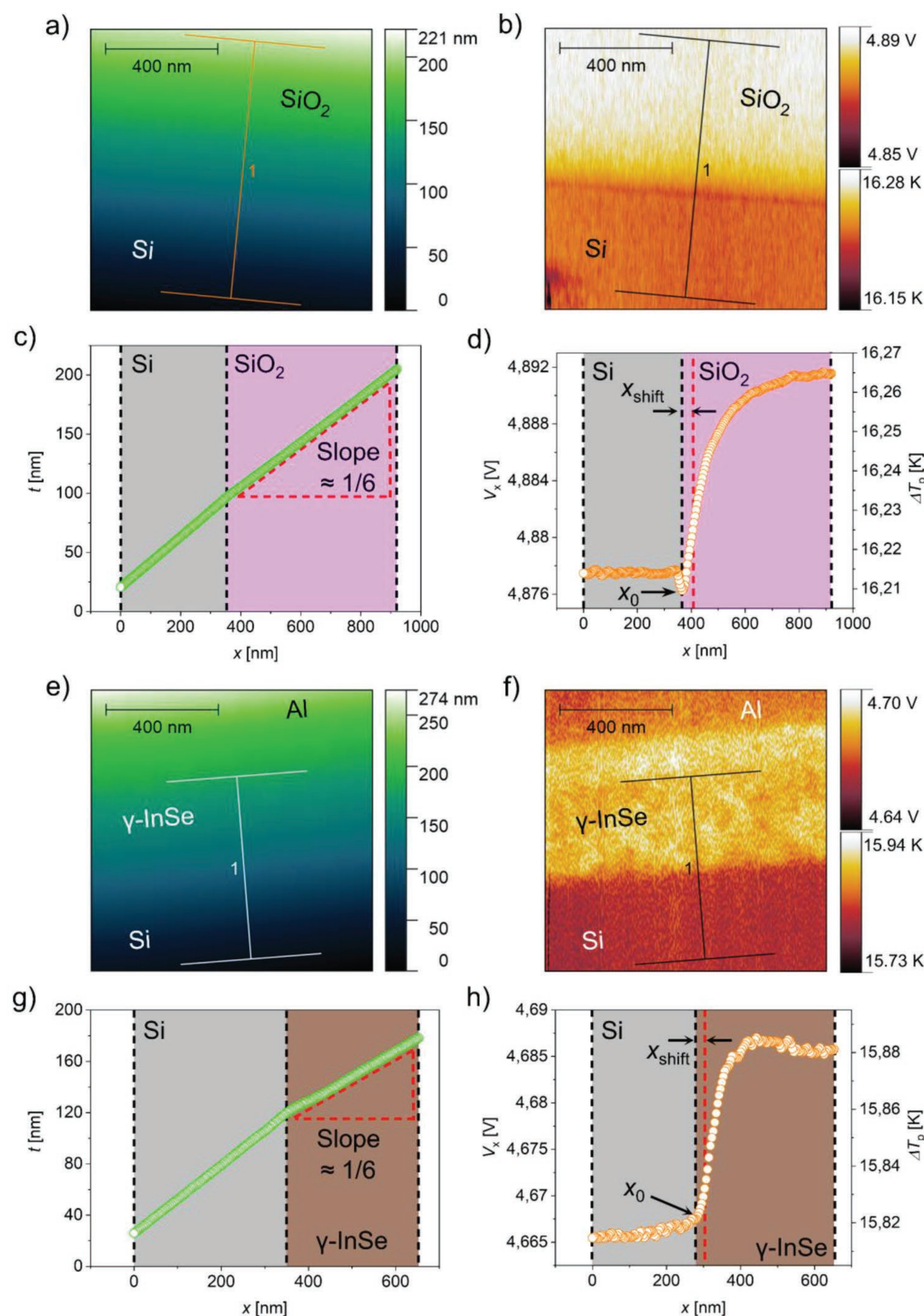

Figure 3. xSThM topography and thermal data. a) Topography and b) thermal signal images of the reference 300 nm SiO_2/Si sample. c) Topography and d) thermal signal profiles taken along the direction 1 of the reference sample maps shown in (a) and (b). e) Topography and f) thermal signal images of the γ-InSe/Si sample. Note that the top aluminum (Al) layer forms as a result of the Ar beam re-sputtering the Al cover of the inner chamber of the BEXP. g) Topography and h) thermal signal profiles taken along the direction 1 of the γ-InSe/Si sample shown in (e) and (f). The high flatness of the BEXP wedge cut in both samples is clear in the topography profiles. The average probe temperature change ΔT_p limits have been added to the thermal maps as a bottom color bar and to the thermal profiles on the right axis for a comparison with the thermal signal.

The data points in the narrow transition zone, which appears due to the final width of the probe, are affected by the transition between the two materials. Therefore, only the data points with thicknesses $t > t_{shift}$ (≈5 nm), corresponding to the tip position greater than the typical tip contact radius (x_{shift} > 30 nm), are used here for the analysis. As a consequence, the thickness range of the γ-InSe flake used for the measurements of the thermal conductivity spans from 5 up to 80 nm, with lateral tip displacement in the range of 30 to 300 nm. In order to reduce the minimum measurable thickness and improve

 © 2023 The Authors. Advanced Materials Interfaces published by Wiley-VCH GmbH

the resolution of the measurements, the tip-sample contact radius would have to be smaller. This can be achieved by both reducing the tip apex radius with a carbon nanotube at the end of the thermal probe as described elsewhere [69] and by doing a gentler post-polishing of the wedge surface in the BEXP (with accelerating voltage down to a few 100 V or post-processing the cut via nanotomography with a stiff SPM tip that can also further remove the remaining surface damage).[70,71] We note that these thicknesses and lateral tip displacements are larger than the corresponding phonon mean free path λ of γ-InSe, which is of the order of 3 nm, as reported elsewhere.[72] The upper bound of the mean free path for γ-InSe can also be estimated using the kinetic model ($\lambda = 3k_z C_v^{-1} \upsilon_s^{-1}$) where υ_s is the speed of sound, C_v is the volumetric heat capacity [73] and k_z are the literature reported thermal conductivity values of layered γ-InSe ($\approx$2 $Wm^{-1} K^{-1}$).[27,41,73] This results in a mean free path $\lambda < 5$ nm. Therefore, for the range of thicknesses involved, it is reasonable to use a diffusion thermal transport approximation for this material and consider that the tip-surface contact thermal resistance R_c and the sample-substrate thermal resistivity r_{int} depend only on the combination of materials and are independent of the thickness. The diffusive-ballistic transport transition represents another limitation of the described method for the sample thicknesses below the mean free path of the heat carriers. While the xSThM will still remain sensitive to the thermal conductivity and its anisotropy, the quantitative measurements would require appropriate analytical and FEA modeling (e.g., using the Boltzmann transport equation) [74] capable of taking into account the ballistic heat transport.

We then can consider the tip-sample thermal resistance $R_x(t)$ as the sum of the contact thermal resistance in the tip-sample interface R_c, which does not depend on the wedge thickness,[52] and the thickness-dependent thermal resistance of the layer-substrate assembly $R_s(t)$, as $R_x(t) = R_s(t) + R_c$ (see detailed scheme in Section S10, Supporting Information).

Both $R_s(t)$ and R_c depend on the tip contact with the sample, which we can approximate as a disk of radius a, with $R_s(t)$ also dependent on the thermal properties of the layered material and the substrate.[49,52] We use the approach developed by Spièce et al.[49] to evaluate the difference between the thermal resistances at thickness t and t_0 with $R_x(t_0)$ value subtracted as $R_{dif}(t) = R_x(t) - R_x(t_0) = R_s(t) - R_s(t_0)$ (with t_0 selected as t_{shift}). In a major development here, such an approach fully eliminates the unknown parameter R_c, drastically simplifying the analysis and eliminating spurious effects such as the local contact roughness and small interfacial thermal resistances in the surface caused by the BEXP cut.[49] While a very thin oxide layer may be formed on the exposed surface of the InSe layer after the cut, it would only affect the interfacial thermal resistance R_c, which is eliminated from the calculations by using our approach. Moreover, the sample was transferred to the xSThM vacuum chamber directly after the BEXP process, reducing the exposure time of the sample to ambient conditions to the minimum and, therefore, significantly decreasing the potential oxidation level of its surface.

The dependence of the thermal signal of the SiO_2 layer on thickness is qualitatively the same as shown in Figure 3d and is determined by the dimensions of the thermal contact a. For small layer thicknesses $t < a$ (0 to $\approx$30 nm), the signal first increases approximately linearly, followed by gradually increasing saturation for layer thicknesses $t \gg a$. We note that we can assume a constant behavior of the phonon scattering and electron-phonon interactions for thick layers ($t > 5$ nm), but this may not be true for $t < 5$ layers ($\approx$4 nm) and/or flakes with an in-plane size smaller than 1–2 µm.[41] For atomically thin flakes, further studies are required. Essentially, the specific dependence of R_x on the layer thickness is significantly affected by the heat transport anisotropy in the layer, changing from a smooth transition for an isotropic material such as SiO_2 to a sharper transition for a material with a high ratio of in-plane to cross-plane thermal conductivity. Such sharp dependence is evident in Figure 3h, which uses the same SThM tip as used for the SiO_2 measurement providing a first hint of the thermal transport anisotropy of γ-InSe, which is quantified using the analytical approach described below.

2.3. "Muzychka–Spièce" Analysis of Anisotropic Thermal Transport

Here, we use the $R_x(t)$ experimental data to find the in-plane and cross-plane thermal conductivities of the γ-InSe layer (k_{xy} and k_z, respectively) on the substrate with thermal conductivity k_s, as well as to estimate the upper bounds of the interfacial thermal resistivity between the top layer and the substrate r_{int} and the tip-sample thermal resistance R_c (see Section S5, Supporting Information).

Due to the low-angle wedge design of the sample, the xSThM thermal conductance and topography data are simultaneously acquired in a single scan, producing the data of $R_x(t)$ in a few minutes. The data is then processed following two steps. First, the data from the reference SiO_2 layer on the Si substrate sample is used to evaluate the contact radius of the tip-surface contact a (essential to determine the anisotropy of the heat conductance) and the dimensionless SThM probe sensitivity constant c_e, which is the ratio of the probe response to the self-heating and heat transferred to the sample. These two parameters are determined in a single fit of the $R_x(t)$ data for the SiO_2/Si layer using the analytical isotropic model described below. As we use the difference of the thermal resistance for thicknesses t and t_0 ($R_x(t) - R_x(t_0)$), we completely eliminate the unknown tip-sample thermal resistance. The values of a and c_e obtained in the first step are then used for fitting the values of k_{xy} and k_z for the γ-InSe/Si sample in the second step, using a modified analytical model for anisotropic heat transport. The first step measurements (SiO_2) were repeated after the γ-InSe measurements to confirm that the contact area was not physically altered. No change of the $R_x(t)$ dependence was observed at the typical range of normal contact forces for both SiO_2 and γ-InSe samples, confirming the stable contact dimensions a defined by the tip apex shape.

As we demonstrate below, in the second step we also estimate the upper bound of the γ-InSe sample-substrate interfacial thermal resistivity, which does not strongly affect the results for k_{xy} and k_z. Thus, at each step, there are effectively only two parameters to fit with a single curve.

© 2023 The Authors. Advanced Materials Interfaces published by Wiley-VCH GmbH

21967350, 0, Downloaded from https://onlinelibrary.wiley.com/doi/10.1002/admi.202300081 by Test, Wiley Online Library on [15/05/2023]. See the Terms and Conditions (https://onlinelibrary.wiley.com/terms-and-conditions) on Wiley Online Library for rules of use; OA articles are governed by the applicable Creative Commons License

21967350, 0, Downloaded from https://onlinelibrary.wiley.com/doi/10.1002/admi.202300081 by Test, Wiley Online Library on [15/05/2023]. See the Terms and Conditions (https://onlinelibrary.wiley.com/terms-and-conditions) on Wiley Online Library for rules of use; OA articles are governed by the applicable Creative Commons License

For isotropic heat transport of a top layer deposited on a substrate (representing the spreading thermal resistance of this material), we use the following fitting expression.[49,53,54,75]

$$R_s(t) = \frac{1}{\pi k a}\int_0^\infty \left[\frac{1 + Ke^{\left(\frac{-2\xi t_{\mathrm{eff}}}{a}\right)}}{1 - Ke^{\left(\frac{-2\xi t_{\mathrm{eff}}}{a}\right)}}\right] J_1(\xi)\sin(\xi)\frac{d\xi}{\xi^2} \tag{2}$$

where k is the top layer isotropic thermal conductivity, J_1 is the Bessel function of the first kind of order 1, and ξ is the integration variable. K and t_{eff} are defined as:

$$K = \left(1 - \frac{k}{k_s}\right) / \left(1 + \frac{k}{k_s}\right) \tag{3}$$

$$t_{\mathrm{eff}} = t + r_{\mathrm{int}k} \tag{4}$$

This model can be applied to fit the SiO_2/Si data where the top SiO_2 layer is isotropic. For the transverse anisotropic γ-InSe/Si sample, Equation (2) is modified to account for the anisotropic heat transport.[53,54] This is done, as shown by Muzychka et al.,[53,54] by scaling the thickness t into an "anisotropic" thickness t_a and the isotropic top layer thermal conductivity k to an average anisotropic thermal conductivity k_a as:

$$t_a = \frac{t}{\sqrt{k_z / k_{xy}}} \tag{5}$$

$$k_a = \sqrt{k_{xy} k_z} \tag{6}$$

Specifically, we first use the experimental (Equation (1)) dependence of $R_x(t) - R_x(t_0)$ and the analytical (Equation (2)) dependence $R_s(t) - R_s(t_0)$ for the SiO_2 sample, finding a and c_e (single curve, two parameters obtained). Then, we use the values of a and c_e determined at the first step and the analytical Equations (2)–(6) describing the anisotropic model to find k_{xy} and k_z for γ-InSe. We note that the interfacial thermal resistivity r_{int} has a minor effect on the result of the fit (see the family of curves in **Figure 4**b) compared with the absolute values of the average thermal conductivity (curves in Figure 4d). More importantly, the variation of the interfacial thermal resistivity does not affect the "bending shape" of the $R_{\mathrm{dif}}(t)$ curves, which is determined by the anisotropy of the thermal transport (Figure 4c).

The "Muzychka–Spièce" analytical model also allows us to understand the details and the trends of how the sample parameters affect the measured thermal resistance R_x. These behaviors are illustrated in a series of plots in Figure 4a–d. In the isotropic case of SiO_2, Figure 4a shows the change in the shape of the $R_{\mathrm{dif}}(t)$ curve with the variation of the probe-sample contact radius a. The increase of the contact radius leads to a smoother dependence on t as well as to the decrease of the overall thermal resistance. One can see that the experimental data indicate that a is between 20 and 30 nm, with precise fitting placing it at a = 22.92 ± 0.28 nm. Figure 4b, at the same time, shows that the interfacial thermal resistivity between SiO_2 and Si does not change the character of the dependence, with multiparametric fitting shown in Figure 4e resulting in a value for r_{int} of $1.48 \times 10^{-9} \pm 0.20 \times 10^{-9}$ Km^2 W^{-1}, similar to the values reported in the literature (≈1 Km^2 W^{-1}) for the SiO_2/Si interface.[76] As the heat conductivity of the SiO_2 thermal oxide layer is well known, the reference sample also allows the determination of the sensitivity coefficient c_e. This factor originates in the difference in the temperature distribution in the SThM sensing resistive element when it is self-heated compared to when the heat is removed at the end of the probe in contact with the sample.[51] The latter results in the localized temperature variation near the probe apex, hence a smaller effect on the overall sensor resistance is reflected by c_e = 8.29 ± 0.11 (see details in Section S6, Supporting Information).

For the anisotropic material, the increase of the layer anisotropic ratio of in-plane to cross-plane thermal conductivities a_r in Figure 4c from 1 (isotropic) to 6 (highly anisotropic) leads to the steeper rise of the thermal resistance followed by a "plateau". Such "plateau" is expected, as, at large layer thickness, the thermal conductance should not depend on the thickness of the layer and the thermal conductivity of the substrate. Such transition happens when the sample thickness becomes much larger than the tip-sample contact radius a, and, as we specified above, its sharpness depends on the heat transport anisotropy of the layer. This matches both the theoretical predictions in the analytical model as well as the FEA simulation. Our analysis shows that, for the anisotropic samples, such transition is sharper. At the same time, the increase of the direction-averaged thermal conductivity k_a results in a monotonous drop in the thermal resistance as seen in Figure 4d without a notable change in the shape. Once the values of a and c_e are determined from the measurement of the reference SiO_2/Si sample, these data are then used to fit the experimental measurement for the γ-InSe/Si sample, which is known to be anisotropic.[41,42,73] The model uses the transformations as in Equations (5) and (6), allowing us to obtain values for r_{int}, k_{xy}, and k_z, with the typical fitting results shown in Figure 4f and **Table 1**. While the quality of this fitting is not as good as in the reference sample, the goodness of fit value ($R^2 > 0.94$) was sufficient to obtain a reasonable confidence interval. The decrease in the fitting efficacy is probably due to the spatial variation of the thermal signal, likely due to step-like structures at the wedge cut of the 2D material, which was also observable in the nanomechanical maps using ultrasonic force microscopy (UFM),[77,78] while they are practically absent in the Si substrate and the SiO_2 layer. Also, this may indicate other heat transport phenomena in anisotropic media such as bulk-to-layer mode conversion or a certain degree of ballistic transport, even for thicknesses above the mean free path. These would require a separate and more detailed study beyond the measurements of the anisotropic thermal conductivities considered here. Significantly, in our measurements and analysis, there was no observed thermal discontinuity at the interface between the substrate and the γ-InSe layer. Moreover, the fitting model is ultimately valid for uniform thermal conductivities, but in this material, this feature is likely to vary with the layer thickness increasing from 2D material to bulk. We acknowledge that further measurements on other materials are needed to fully understand the disagreement after the saturation point between the experimental and fitting curves. Nevertheless, the anisotropic values measured are still reliable given that the range of thicknesses used for the fitting and the introduced weighting factors prioritize the fitting of the initial

 © 2023 The Authors. Advanced Materials Interfaces published by Wiley-VCH GmbH

21967350, 0, Downloaded from https://onlinelibrary.wiley.com/doi/10.1002/admi.202300081 by Test, Wiley Online Library on [15/05/2023]. See the Terms and Conditions (https://onlinelibrary.wiley.com/terms-and-conditions) on Wiley Online Library for rules of use; OA articles are governed by the applicable Creative Commons License

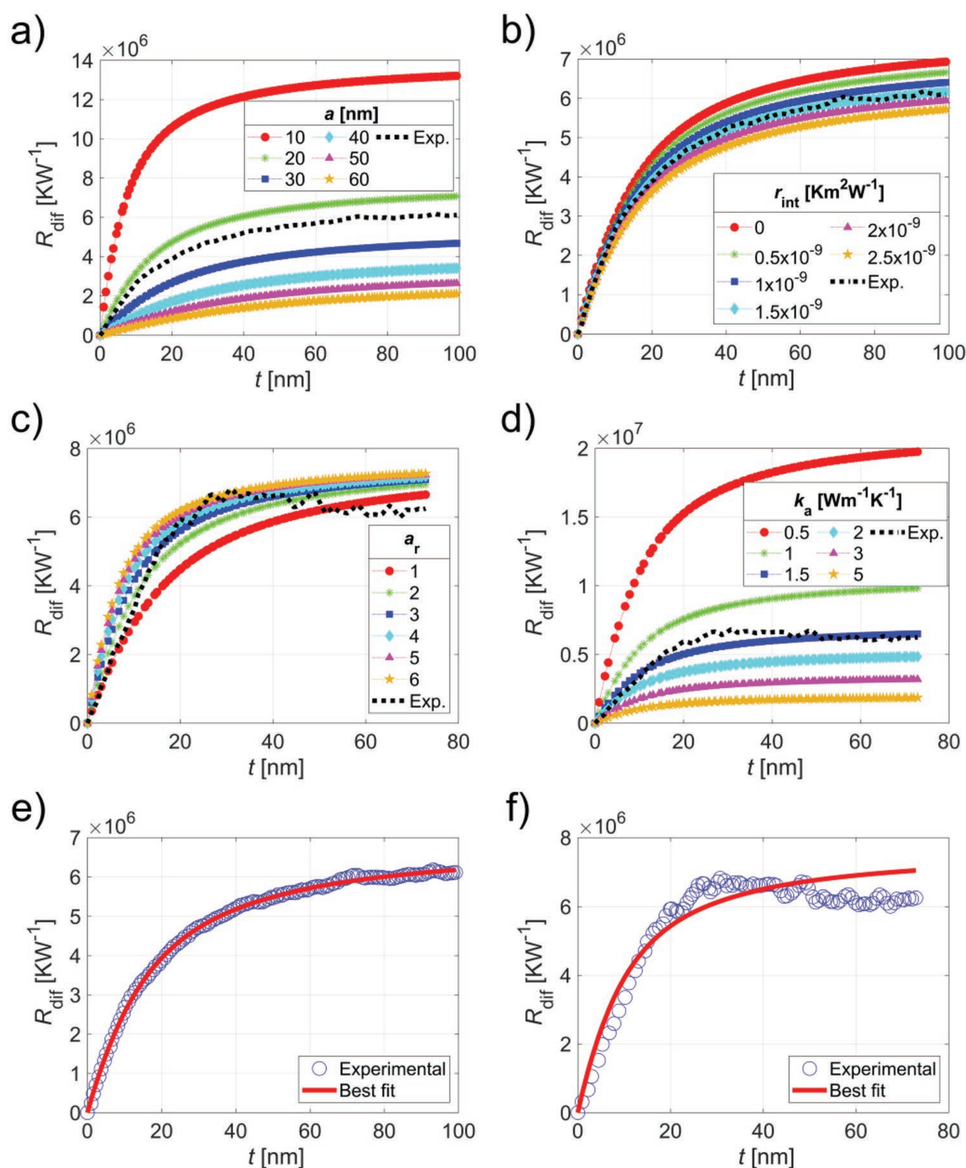

Figure 4. Comparison of simulated dependences of the spreading thermal resistance on the layer thickness $R_{dif}(t)$ according to the "Muzychka–Spièce" model (colored markers) versus experimental (black dotted lines) results for different physical parameters of the tested structures. a) Varying contact radius a. b) Varying interfacial thermal resistivity r_{int}. c) Varying the anisotropic ratio $a_r = k_{xy}k_z^{-1}$ maintaining the anisotropic average thermal conductivity k_a fixed. d) Varying the anisotropic average thermal conductivity k_a maintaining the anisotropic ratio a_r fixed. e) Best fit plot for the SiO_2/Si interface used to obtain a, r_{int}, and c_e. f) Best fit plot for the γ-InSe/Si interface used to obtain r_{int}, k_{xy}, and k_z.

slope and bending area and diminish the saturation influence on this fitting. In fact, these weighting factors have been considered since it is the initial and bending part of the curve that mostly reveals the thermal transport anisotropic degree (as also seen in Figure 4c).

The most significant outcome is that this xSThM approach allows for the first time to obtain direct measurements of both components of the anisotropic thermal conductivity of γ-InSe, with in-plane and cross-plane thermal conductivities of k_{xy} = 2.16 Wm^{-1} K^{-1} and k_z = 0.89 Wm^{-1} K^{-1}, respectively, with

Table 1. Experimental and fitting heat transport parameters of SiO_2 and γ-InSe obtained using xSThM and the "Muzychka–Spièce" model.

Material	a [m]	r_{int} [Km^2 W^{-1}]	c_e	R_c[a] [KW^{-1}]	k_{xy} [Wm^{-1} K^{-1}]	k_z [Wm^{-1} K^{-1}]
SiO_2/Si	$22.92 \times 10^{-9} \pm 0.28 \times 10^{-9}$	1.48×10^{-9}	8.29 ± 0.11	$54.47 \times 10^6 \pm 1.10 \times 10^6$	n/a	n/a
γ-InSe/Si		9.60×10^{-11}		$45.81 \times 10^6 \pm 1.30 \times 10^6$	2.16 ± 0.35	0.89 ± 0.09

[a]See Section S5, Supporting Information.

© 2023 The Authors. Advanced Materials Interfaces published by Wiley-VCH GmbH

ADVANCED MATERIALS INTERFACES
Open Access
www.advmatinterfaces.de

an uncertainty of ≈10%. These values are lower compared to the literature ones [41–42] for bulk crystals of k_{xy} = 10.42 $Wm^{-1} K^{-1}$ and k_z = 1.74 $Wm^{-1} K^{-1}$, possibly due to the effect of the boundaries that may impede phonon transport in the nanoscale flake. As the thermal transport in 2D materials is dominated by phonons, stiffer in-plane covalent bonds result in a higher phonon group velocity and, hence, higher in-plane thermal conductivity compared to the weaker vdW bonds present in the cross-plane direction.[79] The average thermal conductivity (k_a = 1.39 $Wm^{-1} K^{-1}$) is similar to that of SiO_2, being consistent with the qualitative thermal maps in Figure 3. It is interesting to note that the fitted interfacial thermal resistivity between the γ-InSe and the Si layers ($r_{int} = 9.60 \times 10^{-11}$ $Km^2 W^{-1}$) is small, suggesting good thermal contact with the underlying substrate. At the same time, we note that the xSThM thermal conductance is generally not sensitive to thermal resistivities below 10^{-10} $Km^2 W^{-1}$, which can be regarded as an upper boundary of thermal resistivity in this case. This low r_{int} value may have been achieved due to the plasma etching (see Experimental Section), which improved adhesion between the γ-InSe and the Si and removed the majority of the intrinsic thin (≈2–4 Å) native oxide layer on the substrate. Furthermore, several fittings were performed with different r_{int} values. These led to very similar thermal conductivities of γ-InSe, suggesting that this parameter is not critical in the determination of k_{xy} and k_z. More precisely, thermal conductivity has two components, the electronic (k_e) and phononic (k_p) components. Due to the low density of electrons in nominally undoped InSe (carrier density $n \sim 10^{15}$ cm^{-3}),[80] phonons tend to dominate thermal conduction. Additionally, the current implementation of the SThM is mostly sensitive to phononic thermal conductivity.[52] Using Wiedemann–Franz law, we estimate the electronic component $k_e = \sigma LT$, where L is the Lorenz number (2.44×10^{-8} $V^2 K^{-2}$), σ is the material's electrical conductivity and T is the temperature. Here, we have used electron mobility of $\mu = 0.1$ $m^2 V^{-1} s^{-1}$ and $n = 10^{15}$ cm^{-3} to calculate the electrical conductivity as $\sigma = ne\mu$, where e is the carrier's charge value (1.60×10^{-19} C), resulting in $\sigma = 16.02$ Sm^{-1}.[80] At T = 300 K, we estimate $k_e \approx 1 \times 10^{-4}$ $Wm^{-1} K^{-1}$, which is much smaller than the measured thermal conductivity of InSe (> 1 $Wm^{-1} K^{-1}$).

The measurements of the anisotropic thermal conductivity of InSe are directly comparable with similar studies done on other layered materials like Sb_2Te_3/MoS_2 superlattices [67] and perovskites.[81] These provided a similar range of heat parameters with a ratio of in-plane to cross-plane thermal conductivities ranging from 1.0 to 3.0, as well as other layered materials with a higher range of thermal conductivities such as a SiGe composition gradient alloy,[49] furtherly validating our approach.

2.4. Finite Elements Analysis of Heat Transport in the vdW Structure

The analytical results of the "Muzychka–Spièce" measurements of the anisotropic heat transport in the vdW material were also validated using finite element analysis (FEA) simulations. We used COMSOL Multiphysics (see Experimental Section) to simulate heat transport in the wedge-like as well as in the flat layer-on-substrate samples. We confirmed that the thermal resistances of the low-angle wedge sample (3–10°, typical for xSThM) for the values of the thermal conductivities expected for the isotropic SiO_2 and the anisotropic γ-InSe deviate by less than 1% from the resistance values obtained for the flat layer on the substrate (see Section S8, Supporting Information). The flat layer simulation (more computationally efficient) allowed us to explore a whole space of the layer-substrate interfacial thermal resistivity r_{int}, tip-sample contact radius a, and thermal conductivities of the layer (see Section S9, Supporting Information). For the SiO_2 layer, in **Figure 5**a, the experimental R_{dif} curve was located between the simulated 20 and 30 nm contact radius curves, and by using linear interpolation a contact radius of 22 ± 2 nm was obtained, corresponding to exactly the data obtained using the analytical "Muzychka–Spièce" model. By studying the effect of the interfacial thermal resistivity r_{int} (Figure 5b) compared to the other parameters, we confirmed that the interfacial thermal resistivities on the order and below 10^{-9} $Km^2 W^{-1}$ have practically no effect on the total thermal resistance, being consistent with the analytical model. Essentially, for the anisotropic γ-InSe, of both small and larger thicknesses, the heat flow in the structure with the low thermal conductivity substrate, such as SiO_2, is predominantly directed in-plane, while for the higher conductivity substrate (Si), the heat flow does change from cross-plane at low thicknesses to in-plane at layer thicknesses larger than the radius of the contact. It is exactly this transition that allows xSThM to measure independently each component of the anisotropic thermal conductivity of the studied material. Thus, high thermal conductivity substrates such as Si, or more specifically, flat low-roughness substrates with a higher thermal conductivity than the studied material (ideally at least 50% higher), are needed to measure the anisotropy of the thermal transport in anisotropic layered 2D materials (see a more detailed explanation in Section S7, Supporting Information). At the same time, there are no specific requirements for the layered material apart from the thickness and the surface quality of the cut explained above, as well as good thermal contact to ensure the continuity of the temperature at the substrate-layer interface. For instance, transition metal dichalcogenides – bulk materials heterostructures and perovskites nanolayers were effectively studied similarly with the appropriate choice of substrate.[67,81]

While the InSe polytype studied here is the γ-InSe, which has a rhombohedral crystal structure, InSe can also exist in two other polytypes (ε and β), with hexagonal symmetry. This could result in a difference in the thermal transport direction, as the main anisotropy is due to the difference in covalent intralayer bonds versus the weaker vdW interlayer links, as observed in our measurements. To the best of our knowledge, no experimental studies have been conducted targeting the heat transport anisotropy of the ε and β polytypes, with only some reports on the heat transport of composites of the polytypes with other materials.[82–84] At the same time, the study of these materials with the methodology used herein would be of much interest to reveal the details of the anisotropic thermal transport in various InSe polytypes.

In Figure 5c, the experimental γ-InSe/Si data are compared and fitted with the different average top layer thermal conductivities, placing k_a close to 1 $Wm^{-1} K^{-1}$, similar to the analytical solution. For the anisotropic ratio a_r, the "eyeballing" selection of the best-fit curve in Figure 5d is less clear, between

© 2023 The Authors. Advanced Materials Interfaces published by Wiley-VCH GmbH

21967350, 0, Downloaded from https://onlinelibrary.wiley.com/doi/10.1002/admi.202300081 by Test, Wiley Online Library on [15/05/2023]. See the Terms and Conditions (https://onlinelibrary.wiley.com/terms-and-conditions) on Wiley Online Library for rules of use; OA articles are governed by the applicable Creative Commons License

21967350, 0, Downloaded from https://onlinelibrary.wiley.com/doi/10.1002/admi.202300081 by Test, Wiley Online Library on [15/05/2023]. See the Terms and Conditions (https://onlinelibrary.wiley.com/terms-and-conditions) on Wiley Online Library for rules of use; OA articles are governed by the applicable Creative Commons License

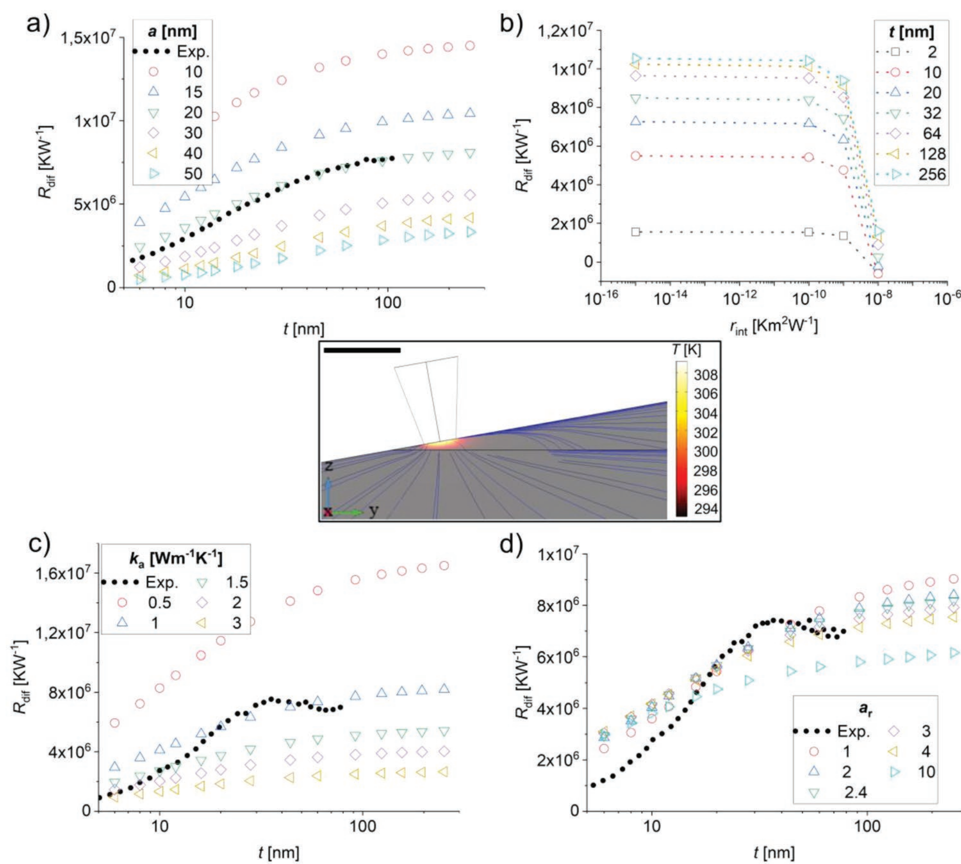

Figure 5. FEA simulation results (hollow markers) versus experimental (filled black circles) results of the contact thermal resistance R_{dif} dependence on the sample thickness t for different physical parameters of a,b) SiO_2/Si and c,d) γ-InSe/Si interfaces. a) Varying contact radius a. b) Varying interfacial thermal resistivity r_{int}. c) Varying anisotropic average thermal conductivity k_a with anisotropic ratio a_r fixed. d) Varying anisotropic ratio a_r with average thermal conductivity k_a fixed. Inset-Heat flow geometry and temperature distribution plot from the FEA simulation. Scale bar 100 nm. (See also Section S9, Supporting Information).

2 and 4, but using the iterative fit, we obtain for the k_a value of 1.4 Wm^{-1} K^{-1} an anisotropic ratio of 2.4. These values are the same as the ones obtained from the fit using the analytical model. We note that, while both approaches provide a similar result, there is a certain deviation between the experimental and calculated data, especially at small thicknesses. This may indicate a deviation of the thermal transport from the diffusive regime as well as a proximity effect of the substrate that requires a different approach beyond the scope of this paper.

3. Conclusion

In summary, here we address an essential need to measure the anisotropic heat transport in the 2D vdW nanostructure γ-InSe, which shows high thermoelectric potential. We used cross-sectional scanning thermal microscopy to independently measure the absolute values of the in-plane and cross-plane thermal conductivities of a vdW flake with a thickness range varying from 5 to 80 nm and evaluate its limits of interfacial thermal resistivity with the supporting substrate. xSThM directly assesses the heat transport of vdW materials on the substrate they are deposited or grown upon without the need for any additional layers to facilitate the measurements. The core of the approach is the measurement of the sample shaped as a low-angle wedge structure using Ar-ion nanopolishing, followed by the mapping of the thermal conductance across the interface between the vdW material and the known substrate using high vacuum SThM. A straightforward analytical model (validated by the detailed FEA simulations) was developed, providing independently the in-plane k_{xy} and cross-plane k_z thermal conductivities of the vdW material and estimating the upper bounds of the thermal resistivity of the vdW material-substrate r_{int}. The approach eliminates a major challenge when using SThM for the nanoscale thermal measurements linked with the unknown probe-sample thermal resistance. We directly obtain absolute values of the anisotropic thermal conductivities for a thin nanoflake of γ-InSe of $k_{xy} = 2.16 \pm 0.35$ Wm^{-1} K^{-1} and $k_z = 0.89 \pm 0.09$ Wm^{-1} K^{-1}, confirming the anomalously low thermal conductivity for this material.

This xSThM approach provides true nanoscale lateral resolution and can be crucial for both understanding the thermal properties of novel vdW materials and their heterostructures as well as for the application of such materials in the heat spreading, thermoelectric and other passive and active nanothermal devices. In particular, by manipulating the thermal conductivity of InSe and other 2D materials via their

 © 2023 The Authors. Advanced Materials Interfaces published by Wiley-VCH GmbH

ADVANCED MATERIALS INTERFACES
Open Access
www.advmatinterfaces.de

heterostructuring [5] and combination of 2D–3D materials' layers [67] and providing a reliable measurement of these, it is possible to create high-performance thermoelectrics for the in-plane and cross-plane operation.

4. Experimental Section

Sample Preparation: The InSe crystals were grown using the Bridgman method from a polycrystalline melt of $In_{1.03}Se_{0.97}$. The crystal structure and γ-phase were assessed by X-ray diffraction studies: the rhombohedral unit cell has lattice parameters of $A = B = 4.002$ Å and $C = 24.961$ Å. The bulk crystals were n-type with a concentration of electrons of 10^{15} cm^{-3}, as determined from Hall effect measurements. γ-InSe thick layers with thicknesses ranging from 0 to ≈100 nm were mechanically exfoliated from the single-crystal bulk material using adhesive film (WF-60/1.5-X4, Gel-Pak) by repeated exfoliation and subsequently deposited on a 10×10 mm^2 chip cleaved from a standard 300 nm SiO_2 wafer. The substrate was primarily activated using Ar/O_2 (98%/2% mix) in plasma cleaner for 15 min to increase adhesion. The flakes were deposited by exfoliation close to the edge of the substrate and baked at 343 K to enhance the contact between the layered material and the substrate. Afterward, beam exit cross-sectional polishing (BEXP) was employed to cut the flakes at a small angle. The technique was performed with a Leica EM TIC 3X triple ion beam cutter system[85] using a custom-made sample stage to achieve a low-angle wedge cut as illustrated in Figure 1. The cutting was performed at different steps, starting with 5 kV for 15 min of warm-up, followed by a 7 kV for 7 h of precise cut, and ending with a post-polishing at 5 kV for 30 min and 1 kV for 1 h.

xSThM Experimental Characterization: The xSThM measurements were performed with an HV NT-MDT scanning thermal microscope with custom-built electronics (see Section S2, Supporting Information) at a pressure of $\approx 2 \times 10^{-6}$ mbar and ambient temperature. A microfabricated Si_3N_4 SThM probe with a resistive palladium (Pd) heater with 0.4 Nm^{-1} spring constant and ≈100 nm tip radius was used at a minimal indentation setpoint to avoid mechanical influence on the scans (KNT-SThM-2an, Kelvin Nanotechnology SThM probe). The probe heater formed part of the balanced Wheatstone bridge that was energized with 3 V DC and 4 V AC voltage with an AC frequency of 91 kHz. The output voltage was measured via a lock-in amplifier (SRS 830), resulting in the xSThM thermal signal proportional to the temperature rise of the probe due to Joule heating with respect to ambient temperature (see details of the calibration in Section S1, Supporting Information).

Finite Element Analysis (FEA) Modelling: For the finite element simulation, COMSOL Multiphysics 5.6 software was used with the heat transfer module. Two geometries of the low-angle wedge as well as a single flat layer on the substrate were used. The comparison had shown that both models produced identical results for the wide range of the layer thermal conductivities (from 0.5 to 10 Wm^{-1} K^{-1}) within a 1% deviation. Several mesh sizes were used and it was confirmed that the difference between them falls well within this error limit. Then, the single-layer model was used to simulate the thermal resistance of the sample for the multiparametric simulation, varying sample thickness from 2 to 256 nm, averaged thermal conductivity k_a from 0.5 to 10 Wm^{-1} K^{-1}, thermal anisotropy coefficient a_r from 1 to 10 and several values of the interfacial thermal resistivity from very low to 10^{-8} Km^2 W^{-1} (for details see Sections S3 and S8, Supporting Information).

Statistical Analysis: The data from the xSThM scans were processed only via offset flattening and noise elimination. The sample size was a reference SiO_2 on Si structure for the isotropic and calibration measurements and a γ-InSe on Si sample for the main measurements and analysis.

Supporting Information

Supporting Information is available from the Wiley Online Library or from the author.

Acknowledgements

The authors are grateful to Dr. Charalambos Evangeli from the University of Oxford and Dr. Yue Chen and Dr. Alexander Robson from Lancaster University for an insightful discussion on the SThM and BEXP measurements. The authors also acknowledge the financial and technical support from Bruker, NT-MDT, and LEICA Microsystems. The support of the European Commission Graphene Flagship Core project 3 (grant agreement no. 881603), NPL Quantum Programme (BEIS), EPSRC EP/V00767X/1 HiWiN project, UKRI Faraday Institution NEXGENNA project (grant number FIRG018), and Paul Instrument Fund (c/o The Royal Society) is fully appreciated.

Conflict of Interest

The authors declare no conflict of interest.

Author Contributions

S.G.M., O.V.K., K.A., and E.G.C. conceived the study, the development steps, and its realization. Z.D.K. and Z.R.K. synthesized the bulk γ-InSe crystal. Z.R.K., O.K., and A.P. provided the analysis of the γ-InSe sample structure, physical behavior, and nanoscale heat transport. S.G.M. prepared the γ-InSe/Si sample with the help of E.G.C. and performed the BEXP cut on SiO_2/Si and γ-InSe/Si samples. S.G.M., K.A., E.G.C., and O.V.K. performed the xSThM measurements on both samples. K.A. performed the probe calibration, the ambient V_{nc} measurements, and, jointly with E.G.C. and S.G.M., the flat layers measurements. S.G.M. performed the data analysis and analytical modeling with the contribution of J.S., O.V.K., and K.A. S.G.M. and O.V.K. performed the FEA modeling. S.G.M., O.V.K., and K.A. provided the interpretation of the obtained results from the experiments, the analytical model, and the FEA simulation. S.G.M. provided the initial draft of the manuscript. All authors contributed to the discussions and modification of the draft, its final version, and a revision.

Data Availability Statement

The data that support the findings of this study are available from the corresponding author upon reasonable request.

Keywords

cross-sectional scanning thermal microscopy, gamma indium selenide, nanoscale heat transport, thermal conductivity anisotropy, van der Waals materials

Received: January 30, 2023
Revised: March 21, 2023
Published online:

[1] D. Akinwande, C. J. Brennan, J. S. Bunch, P. Egberts, J. R. Felts, H. Gao, R. Huang, J.-S. Kim, T. Li, Y. Li, K. M. Liechti, N. Lu, H. S. Park, E. J. Reed, P. Wang, B. I. Yakobson, T. Zhang, Y.-W. Zhang, Y. Zhou, Y. Zhu, *Extreme Mech. Lett.* **2017**, *13*, 42.
[2] M. Bernardi, C. Ataca, M. Palummo, J. C. Grossman, *Nanophotonics* **2017**, *6*, 479.
[3] H. Wang, G. Qin, G. Li, Q. Wang, M. Hu, *Phys. Chem. Chem. Phys.* **2017**, *19*, 12882.
[4] Z. Tong, T. Dumitrică, T. Frauenheim, *Nano Lett.* **2021**, *21*, 4351.

© 2023 The Authors. Advanced Materials Interfaces published by Wiley-VCH GmbH

21967350, 0, Downloaded from https://onlinelibrary.wiley.com/doi/10.1002/admi.202300081 by Test, Wiley Online Library on [15/05/2023]. See the Terms and Conditions (https://onlinelibrary.wiley.com/terms-and-conditions) on Wiley Online Library for rules of use; OA articles are governed by the applicable Creative Commons License

[5] K. S. Novoselov, A. Mishchenko, A. Carvalho, A. H. Castro Neto, *Science* **2016**, *353*, aac9439.
[6] B. V. Lotsch, *Annu. Rev. Mater. Res.* **2015**, *45*, 85.
[7] K. S. Novoselov, D. Jiang, F. Schedin, T. J. Booth, V. V. Khotkevich, S. V. Morozov, A. K. Geim, *Proc. Natl. Acad. Sci. U. S. A.* **2005**, *102*, 10451.
[8] K. S. Novoselov, A. K. Geim, S. V. Morozov, D. Jiang, Y. Zhang, S. V. Dubonos, I. V. Grigorieva, A. A. Firsov, *Science* **2004**, *306*, 666.
[9] X.-Y. Fang, X.-X. Yu, H.-M. Zheng, H.-B. Jin, L. Wang, M.-S. Cao, *Phys. Lett. A* **2015**, *379*, 2245.
[10] R. S. Chen, C. C. Tang, W. C. Shen, Y. S. Huang, *Nanotechnology* **2014**, *25*, 9.
[11] S. Zhou, X. Tao, Y. Gu, *J. Phys. Chem. C* **2016**, *120*, 4753.
[12] W. Jang, Z. Chen, W. Bao, C. N. Lau, C. Dames, *Nano Lett.* **2010**, *10*, 3909.
[13] B. J. Robinson, C. E. Giusca, Y. T. Gonzalez, N. D. Kay, O. Kazakova, O. V. Kolosov, *2D Mater.* **2015**, *2*, 015005.
[14] L. M. Sandonas, G. Cuba-Supanta, R. Gutierrez, A. Dianat, C. V. Landauro, G. Cuniberti, *Carbon* **2017**, *124*, 642.
[15] Z. Lin, A. McNamara, Y. Liu, K.-s. Moon, C.-P. Wong, *Compos. Sci. Technol.* **2014**, *90*, 123.
[16] E. Fleming, I. Kholmanov, L. Shi, *Carbon* **2018**, *136*, 380.
[17] Z. Zhang, S. Hu, J. Chen, B. Li, *Nanotechnology* **2017**, *28*, 225704.
[18] H. G. Zhang, H. Y. Wang, S. Y. Xiong, H. X. Han, S. T. Volz, Y. X. Ni, *J. Phys. Chem. C* **2018**, *122*, 2641.
[19] A. Soudi, R. D. Dawson, Y. Gu, *ACS Nano* **2011**, *5*, 255.
[20] M. Zare, B. Z. Rameshti, F. G. Ghamsari, R. Asgari, *Phys. Rev. B* **2017**, *95*, 045422.
[21] Y. Xu, Z. Y. Li, W. H. Duan, *Small* **2014**, *10*, 2182.
[22] J. Wu, Y. B. Chen, J. Q. Wu, K. Hippalgaonkar, *Adv. Electron. Mater.* **2018**, *4*, 1800248.
[23] I. Pallecchi, N. Manca, B. Patil, L. Pellegrino, D. Marre, *Nano Futures* **2020**, *4*, 032008.
[24] T. A. Amollo, G. T. Mola, M. S. K. Kirui, V. O. Nyamori, *Crit. Rev. Solid State Mater. Sci.* **2018**, *43*, 133.
[25] K. F. Mak, C. Lee, J. Hone, J. Shan, T. F. Heinz, *Phys. Rev. Lett.* **2010**, *105*, 136805.
[26] S. Hasegawa, F. Grey, *Surf. Sci.* **2002**, *500*, 84.
[27] Y. Zhao, Y. Cai, L. Zhang, B. Li, G. Zhang, J. T. L. Thong, *Adv. Funct. Mater.* **2020**, *30*, 1903929.
[28] C.-H. Ho, H.-H. Chen, *Sci. Rep.* **2014**, *4*, 6143.
[29] S. Xie, A. Dey, W. Yan, Z. R. Kudrynskyi, N. Balakrishnan, O. Makarovsky, Z. D. Kovalyuk, E. G. Castanon, O. Kolosov, K. Wang, A. Patanè, *2D Mater.* **2021**, *8*, 045020.
[30] C.-H. Ho, *Sci. Rep.* **2014**, *4*, 4764.
[31] C.-H. Ho, M.-H. Lin, Y.-P. Wang, Y.-S. Huang, *Sens. Actuators, A* **2016**, *245*, 119.
[32] Q. Zhao, R. Frisenda, T. Wang, A. Castellanos-Gomez, *Nanoscale* **2019**, *11*, 9845.
[33] Y. Li, C. Yu, Y. Gan, Y. Kong, P. Jiang, D.-F. Zou, P. Li, X.-F. Yu, R. Wu, H. Zhao, C.-F. Gao, J. Li, *Nanotechnology* **2019**, *30*, 335703.
[34] W. J. Ding, J. B. Zhu, Z. Wang, Y. F. Gao, D. Xiao, Y. Gu, Z. Y. Zhang, W. G. Zhu, *Nat. Commun.* **2017**, *8*, 14956.
[35] G. W. Mudd, S. A. Svatek, T. Ren, A. Patanè, O. Makarovsky, L. Eaves, P. H. Beton, Z. D. Kovalyuk, G. V. Lashkarev, Z. R. Kudrynskyi, A. I. Dmitriev, *Adv. Mater.* **2013**, *25*, 5714.
[36] J. F. Sánchez-Royo, G. Muñoz-Matutano, M. Brotons-Gisbert, J. P. Martínez-Pastor, A. Segura, A. Cantarero, R. Mata, J. Canet-Ferrer, G. Tobias, E. Canadell, J. Marqués-Hueso, B. D. Gerardot, *Nano Res.* **2014**, *7*, 1556.
[37] K. Li, Y. Hong, Z. Li, X. Liu, *Appl. Phys. Lett.* **2018**, *113*, 021903.
[38] S. R. Tamalampudi, Y.-Y. Lu, R. U. Kumar, R. Sankar, C.-D. Liao, K. B. Moorthy, C.-H. Cheng, F. C. Chou, Y.-T. Chen, *Nano Lett.* **2014**, *14*, 2800.
[39] C. Song, S. Huang, C. Wang, J. Luo, H. Yan, *J. Appl. Phys.* **2020**, *128*, 060901.
[40] W. Feng, W. Zheng, W. Cao, P. Hu, *Adv. Mater.* **2014**, *26*, 6587.
[41] D. Buckley, Z. R. Kudrynskyi, N. Balakrishnan, T. Vincent, D. Mazumder, E. Castanon, Z. D. Kovalyuk, O. Kolosov, O. Kazakova, A. Tzalenchuk, A. Patanè, *Adv. Funct. Mater.* **2021**, *31*, 2008967.
[42] S. M. Atakishiev, D. S. Abdinov, G. A. Akhundov, *Phys. Status Solidi B* **1968**, *28*, K47.
[43] H. Zhou, Y. Cai, G. Zhang, Y. W. Zhang, *Nanoscale* **2018**, *10*, 480.
[44] D. A. Bandurin, A. V. Tyurnina, G. L. Yu, A. Mishchenko, V. Zólyomi, S. V. Morozov, R. K. Kumar, R. V. Gorbachev, Z. R. Kudrynskyi, S. Pezzini, Z. D. Kovalyuk, U. Zeitler, K. S. Novoselov, A. Patanè, L. Eaves, I. V. Grigorieva, V. I. Fal'ko, A. K. Geim, Y. Cao, *Nat. Nanotechnol.* **2017**, *12*, 223.
[45] Y. Zhang, W. Zhu, F. Hui, M. Lanza, T. Borca-Tasciuc, M. M. Rojo, *Adv. Funct. Mater.* **2019**, *30*, 1900892.
[46] S. Gomès, A. Assy, P.-O. Chapuis, *Phys. Status Solidi A* **2015**, *212*, 477.
[47] A. Majumdar, *Annu. Rev. Mater. Sci.* **1999**, *29*, 505.
[48] P. Tovee, M. Pumarol, D. Zeze, K. Kjoller, O. Kolosov, *J. Appl. Phys.* **2012**, *112*, 114317.
[49] J. Spièce, C. Evangeli, A. J. Robson, A. El Sachat, L. Haenel, M. I. Alonso, M. Garriga, B. J. Robinson, M. Oehme, J. Schulze, F. Alzina, C. Sotomayor Torres, O. V. Kolosov, *Nanoscale* **2021**, *13*, 10829.
[50] S. Poon, J. Spièce, A. Robson, O. V. Kolosov, S. Thompson, presented at *2017 IEEE Int. Magnetics Conf. (INTERMAG)*, Dublin, Ireland, April **2017**.
[51] J. Spiece, C. Evangeli, K. Lulla, A. Robson, B. Robinson, O. Kolosov, *J. Appl. Phys.* **2018**, *124*, 015101.
[52] C. Evangeli, J. Spiece, S. Sangtarash, A. J. Molina-Mendoza, M. Mucientes, T. Mueller, C. Lambert, H. Sadeghi, O. Kolosov, *Adv. Electron. Mater.* **2019**, *5*, 1900331.
[53] Y. S. Muzychka, M. M. Yovanovich, J. R. Culham, *J. Thermophys. Heat Transfer* **2004**, *18*, 45.
[54] Y. S. Muzychka, *J. Thermophys. Heat Transfer* **2014**, *28*, 313.
[55] O. V. Kolosov, I. Grishin, R. Jones, *Nanotechnology* **2011**, *22*, 185702.
[56] I. Grishin, B. D. Huey, O. V. Kolosov, *ACS Appl. Mater. Interfaces* **2013**, *5*, 11441.
[57] J. L. Bosse, I. Grishin, B. D. Huey, O. V. Kolosov, *Appl. Surf. Sci.* **2014**, *314*, 151.
[58] A. J. Robson, I. Grishin, R. J. Young, A. M. Sanchez, O. V. Kolosov, M. Hayne, *ACS Appl. Mater. Interfaces* **2013**, *5*, 3241.
[59] M. Timofeeva, A. Bolshakov, P. D. Tovee, D. A. Zeze, V. G. Dubrovskii, O. V. Kolosov, *Ultramicroscopy* **2016**, *162*, 42.
[60] P. Janus, D. Szmigiel, M. Weisheit, G. Wielgoszewski, Y. Ritz, P. Grabiec, M. Hecker, T. Gotszalk, P. Sulecki, E. Zschech, *Microelectron. Eng.* **2010**, *87*, 1370.
[61] E. Gmelin, R. Fischer, R. Stitzinger, *Thermochim. Acta* **1998**, *310*, 1.
[62] P. S. Dobson, J. M. R. Weaver, G. Mills, in *New Methods for Calibrated Scanning Thermal Microscopy (SThM), Sensors, 2007*, IEEE, Atlanta, GA **2007**, p. 708, https://doi.org/10.1109/icsens.2007.4388498.
[63] W. Zhu, G. Zheng, S. Cao, H. He, *Sci. Rep.* **2018**, *8*, 10537.
[64] F. R. Brotzen, P. J. Loos, D. P. Brady, *Thin Solid Films* **1992**, *207*, 197.
[65] H. R. Shanks, P. D. Maycock, P. H. Sidles, G. C. Danielson, *Phys. Rev.* **1963**, *130*, 1743.
[66] X. Li, Y. Yan, L. Dong, J. Guo, A. Aiyiti, X. Xu, B. Li, *J. Phys. D: Appl. Phys.* **2017**, *50*, 104002.
[67] M. Ahmad, K. Agarwal, S. G. Munoz, A. Ghosh, N. Kodan, O. V. Kolosov, B. R. Mehta, *Adv. Funct. Mater.* **2022**, *32*, 2206384.
[68] J. L. Bosse, M. Timofeeva, P. D. Tovee, B. J. Robinson, B. D. Huey, O. V. Kolosov, *J. Appl. Phys.* **2014**, *116*, 134904.
[69] P. D. Tovee, M. E. Pumarol, M. C. Rosamond, R. Jones, M. C. Petty, D. A. Zeze, O. V. Kolosov, *Phys. Chem. Chem. Phys.* **2014**, *16*, 1174.
[70] J. Song, Y. Zhou, N. P. Padture, B. D. Huey, *Nat. Commun.* **2020**, *11*, 3308.

© 2023 The Authors. Advanced Materials Interfaces published by Wiley-VCH GmbH

21967350, 0, Downloaded from https://onlinelibrary.wiley.com/doi/10.1002/admi.202300081 by Test, Wiley Online Library on [15/05/2023]. See the Terms and Conditions (https://onlinelibrary.wiley.com/terms-and-conditions) on Wiley Online Library for rules of use; OA articles are governed by the applicable Creative Commons License

[71] W. Zhang, Y. Chen, C. Xu, C. Lin, J. Tao, Y. Lin, J. Li, O. V. Kolosov, Z. Huang, *Nano Energy* **2023**, *108*, 108199.
[72] H. Shi, D. Wang, Y. Xiao, L.-D. Zhao, *Aggregate* **2021**, *2*, 92.
[73] A. Rai, V. K. Sangwan, J. T. Gish, M. C. Hersam, D. G. Cahill, *Appl. Phys. Lett.* **2021**, *118*, 073101.
[74] H. L. Li, B. Y. Cao, *Nanoscale Microscale Thermophys. Eng.* **2019**, *23*, 10.
[75] M. M. Yovanovich, J. R. Culham, P. Teertstra, *IEEE Trans. Compon., Packag., Manuf. Technol., Part A* **1998**, *21*, 168.
[76] J. Chen, G. Zhang, B. Li, *J. Appl. Phys.* **2012**, *112*, 064319.
[77] N. Tapia-Ruiz, A. R. Armstrong, H. Alptekin, M. A. Amores, H. Au, J. Barker, R. Boston, W. R. Brant, J. M. Brittain, Y. Chen, M. Chhowalla, Y.-S. Choi, S. I. R. Costa, M. Crespo Ribadeneyra, S. A. Cussen, E. J. Cussen, W. I. F. David, A. V. Desai, S. A. M. Dickson, E. I. Eweka, J. D. Forero-Saboya, C. P. Grey, J. M. Griffin, P. Gross, X. Hua, J. T. S. Irvine, P. Johansson, M. O. Jones, M. Karlsmo, E. Kendrick, et al., *JPhys Energy* **2021**, *3*, 031503.
[78] J. L. Bosse, P. D. Tovee, B. D. Huey, O. V. Kolosov, *J. Appl. Phys.* **2014**, *115*, 144304.
[79] F. Vialla, N. Del Fatti, *Nanomaterials* **2020**, *10*, 2543.
[80] A. V. Zaslonkin, V. M. Kaminskii, Z. D. Kovalyuk, I. V. Mintyanskii, M. V. Tovarnitskii, *Inorg. Mater.* **2006**, *42*, 1308.
[81] A. Maiti, K. Agarwal, S. Gonzalez-Munoz, O. V. Kolosov, *Phys. Rev. Mater.* **2023**, *7*, 023801.
[82] B. Zhang, H. Wu, K. Peng, X. Shen, X. Gong, S. Zheng, X. Lu, G. Wang, X. Zhou, *Chin. Phys. B* **2021**, *30*, 078101.
[83] V. D. Botcha, M. Zhang, K. Li, H. Gu, Z. Huang, J. Cai, Y. Lu, W. Yu, X. Liu, *J. Alloys Compd.* **2018**, *735*, 594.
[84] D. K. Sang, H. Wang, M. Qiu, R. Cao, Z. Guo, J. Zhao, Y. Li, Q. Xiao, D. Fan, H. Zhang, *Nanomaterials* **2019**, *9*, 82.
[85] Leica Microsystems, Ion Beam Milling System Leica EM TIC 3X, https://www.leica-microsystems.com/products/sample-preparation-for-electron-microscopy/p/leica-em-tic-3x/ (accessed: May **2022**).

© 2023 The Authors. Advanced Materials Interfaces published by Wiley-VCH GmbH

21967350, 0, Downloaded from https://onlinelibrary.wiley.com/doi/10.1002/admi.202300081 by Test, Wiley Online Library on [15/05/2023]. See the Terms and Conditions (https://onlinelibrary.wiley.com/terms-and-conditions) on Wiley Online Library for rules of use; OA articles are governed by the applicable Creative Commons License